



Ultra-low-power nonvolatile integrated photonic switches and modulators based on nanogap-enhanced phase-change waveguides

JIEYING ZHANG,^{1,2} JIAJIU ZHENG,³  PEIPENG XU,^{1,2,5}  YANQUN WANG,^{1,2} AND ARKA MAJUMDAR^{3,4,6} 

¹Faculty of Electrical Engineering and Computer Science, Ningbo University, Ningbo 315211, China

²Key Laboratory of Photoelectric Detection Materials and Devices of Zhejiang Province, Ningbo 315211, China

³Department of Electrical and Computer Engineering, University of Washington, Seattle, WA 98195, USA

⁴Department of Physics, University of Washington, Seattle, WA 98195, USA

⁵xupeipeng@nbu.edu.cn

⁶arka@uw.edu

Abstract: We propose a nanogap-enhanced phase-change waveguide with silicon PIN heaters. Thanks to the enhanced light-matter interaction in the nanogap, the proposed structure exhibits strong attenuation ($\Delta\alpha = \sim 35$ dB/ μm) and optical phase ($\Delta n_{\text{eff}} = \sim 1.2$) modulation at $\lambda = 1550$ nm when achieving complete phase transitions. We further investigate two active optical devices based on the proposed waveguide, including an electro-absorption modulator and a 1×2 directional-coupler optical switch. Finite-difference time-domain simulation of the proposed modulator shows a high extinction ratio of ~ 17 dB at 1550 nm with an active segment of volume only $\sim 0.004\lambda^3$. By exploiting a directional coupler design, we present a 1×2 optical switch with an insertion loss of < 4 dB and a compact coupling length of ~ 15 μm while maintaining small crosstalk less than -7.2 dB over an optical bandwidth of 50 nm. Thermal analysis shows that a 10 V pulse of 30 ns (1×1 modulator) and 55 ns (1×2 switch) in duration is required to raise the GST temperature of the phase-change waveguide above the melting temperature to induce the amorphization; however, the complete crystallization occurs by applying a 5 V pulse of 180 ns (1×1 modulator) and a 6 V pulse of 200 ns (1×2 switch), respectively.

© 2020 Optical Society of America under the terms of the [OSA Open Access Publishing Agreement](#)

1. Introduction

Despite the impressive progress of electronics in data processing and storage as well as logic operations, photonic integrated circuits (PICs) are becoming more and more attractive by offering broad bandwidth with energy-efficient information transport, processing, and storage [1,2]. Silicon photonics is regarded as one of the most promising technologies to realize large-scale PICs, having multiple advantages over other substrate materials [3]. The most remarkable is the compatibility with the already well-developed CMOS technology and the high index contrast. The former leads to scalability and low fabrication cost and the latter to higher optical confinement and, therefore, to high-density integration. To realize reconfigurable photonic systems, active components such as modulators and switches are essential to control the light flow within the network [4,5]. These devices need to have high performance, such as low loss, high switching contrast, as well as low static and dynamic power consumption to satisfy the system demands.

Current switches and modulators in silicon photonics utilizing the configurations of Mach-Zehnder interferometer [4–6] (wide operational bandwidth) and micro-ring resonator [7] (high modulation strength but intrinsic narrow optical bandwidth and high sensitivity to fabrication imperfections), primarily rely on electro-optic effect by using carrier injection or depletion in a P-I-N or P-N diode structure or thermo-optic effect by locally heating silicon waveguides [8,9].

However, both effects suffer from the weak modulation of the refractive index (usually $\Delta n < 0.01$), leading to high energy consumption and large footprints. Moreover, as the switching mechanism is volatile, a constant power supply is required to maintain the switched state. Therefore, it is highly desirable to explore a nonvolatile optical switch that necessitates no continuous power supply and, at the same time, feature compelling performances in the loss, extinction ratios, and size.

Recently, chalcogenide phase-change materials (PCMs) such as $\text{Ge}_2\text{Sb}_2\text{Te}_5$ (GST) have been developed to provide strong modulation and nonvolatility for on-chip optical modulators and switches due to several unique properties [10]. First, PCMs are stable (years at room temperature) in both amorphous or crystalline states with the large contrast in optical constants (usually $\Delta n > 1$) [11,12], leading to intense phase or amplitude modulation within a small device footprint. The crucial feature of integrated photonic PCM-based devices is so-called “self-holding”, meaning that energy is only consumed during the actual switching process [13,14]. Third, the state can be quickly and reversibly changed by nanosecond light or electrical pulses with potentially long endurance up to 10^{15} cycles [15,16]. Consequently, PCMs have already been integrated directly on silicon photonic waveguides to implement arithmetic processing, in-memory computing, and neuromorphic computing [17–19], in which the essential operation is nonvolatile and reversible switching [20–30].

Slot or nanogap waveguide, whereby the discontinuity of the optical field at a dielectric interface was exploited, was exploited to provide light field confinement in a nanometer-wide low-index material, thereby enhancing the light-matter interaction dramatically [31]. The use of such a concept has garnered a considerable interest in the recent years, for applications including dispersion engineering [32,33], nonlinear enhancement [34,35], and optical sensing [36,37].

In this work, we propose a nonvolatile nanogap-enhanced phase-change waveguide with GST in the gap, realizing an ultra-small non-resonant and high static performance switch. Considering the effective area of the GST used in the nanogap phase-change waveguides, the proposed structures exhibit a high energy efficiency of 64 aJ/nm^3 (36 aJ/nm^3) while achieving complete crystallization (amorphization) transitions, which is half of that in PCM-clad silicon waveguides [38].

2. Structure and design

Figure 1 shows the cross section of the proposed nanogap enhanced phase-changed waveguide. A GST layer is vertically sandwiched between two Si waveguide sections to form a nanogap enhanced phase-change waveguides. The overall width of the waveguide and the width of the GST segment is set to be w_{si} and w_{gst} , respectively. Here the height of the silicon layer is set to be $h_{\text{si}} = 250 \text{ nm}$, which is a standard value for silicon-on-insulator (SOI) wafers. To conduct the electrical switching, a thin pedestal layer with a thickness of $h_s = 50 \text{ nm}$ and two highly doped regions along with metallic contacts on top of them are also considered in the waveguide cross

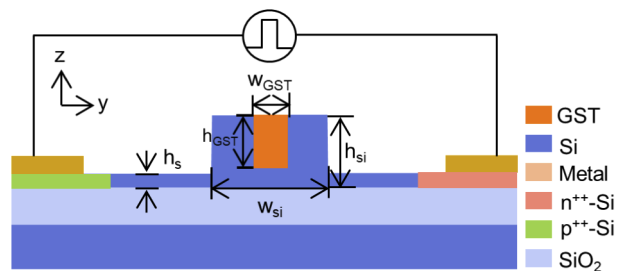


Fig. 1. The cross section of the proposed nanogap enhanced phase-change waveguide.

section. To form the silicon PIN diode (p-type, intrinsic, n-type junction) heaters, the slab is heavily doped by boron and phosphorus ion implantation, in which the doping concentration is chosen as 10^{20} cm^{-3} to achieve high conductivity. The separation distance away from the edge of the rib in the active region is chosen to be $1 \mu\text{m}$ to reduce the resistance, but still far enough from the supporting mode distribution to ensure a negligible optical loss. Here we choose h_{GST} to be 200 nm to facilitate the electrical switching. The nanogap waveguide structures could be fabricated on silicon by standard electron-beam lithography (EBL) and dry etching process. The p++ (n++) doping and metal deposition can be conducted by conventional protocols previously reported [39]. Then, another EBL step could be implemented to define window for GST deposition. Last, a stack of GST was deposited using RF sputtering followed by a lift-off process.

Optical characteristics of the proposed nanogap phase-change hybrid waveguide depend on the phase of the GST. A full vectorial mode solver based on the finite element method (COMSOL Multiphysics) has been used to calculate the guided mode. Figures 2(a)–2(b) show the Poynting vector for the fundamental quasi-transverse magnetic (TM) mode with amorphous GST (aGST) and crystalline GST (cGST) at a wavelength of 1550 nm . Substantial modification of the mode profile and the complex effective index ($\tilde{n}_{\text{eff}} = n_{\text{eff}} - \kappa_{\text{eff}} i$) can be observed once the GST is electrically switched between the amorphous and crystalline states, indicating the substantial refractive and absorptive modulation effects. When GST is in its amorphous phase, the field profile of the proposed waveguide is quite similar to that of a silicon ridge waveguide, with 64.5% of the power distributed in the Si part and only 15.6% of the power lies in the GST part. Once the GST is triggered from the amorphous to the crystalline phase, as shown in Fig. 2(b), the field confinement in the lossy GST is dramatically enlarged to 54.2% due to the considerable refractive index contrast, indicating ultra-strong GST-light interaction. Thus, the effective index difference Δn_{eff} of the fundamental modes of the proposed waveguide upon phase transition is ~ 1.2 which is 6 times of that in the traditional PCM-clad waveguide [38]. The imaginary part of the \tilde{n}_{eff} of the TM mode is increased by a factor of 198. The attenuation coefficient of the hybrid waveguide for the amorphous and crystalline phases are therefore $\sim 0.2 \text{ dB}/\mu\text{m}$ and $\sim 35 \text{ dB}/\mu\text{m}$, respectively. Thus, an electrical pulse applied to the active GST segment can drastically change the optical phase and absorption coefficient of the waveguide.

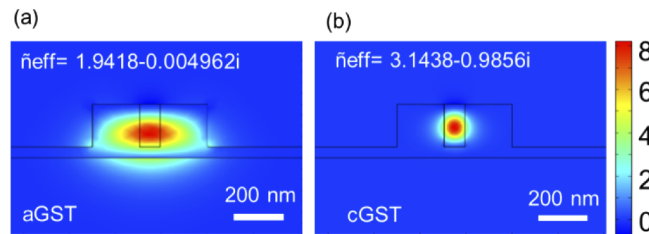


Fig. 2. Spatial distribution of Poynting vector and complex effective index (\tilde{n}_{eff}) of the fundamental quasi-transverse magnetic (TM) mode of the nanogap phase-change waveguide with (a) aGST and (b) cGST ($\lambda = 1550 \text{ nm}$). The width of the GST and the silicon waveguide are $w_{\text{gst}} = 70 \text{ nm}$ and $w_{\text{si}} = 450 \text{ nm}$, respectively.

For nonvolatile phase-change optical switches and modulators, strong optical phase or attenuation modulation and low insertion loss are essential for the optimal performance of the hybrid waveguides. Here, we define an optical figure of merit $\text{FOM1} = \Delta\alpha / \alpha_{\text{agst}}$, where $\Delta\alpha$ denotes the optical attenuation change of the hybrid waveguide upon phase transition, while α_{agst} is the optical attenuation with aGST that determines the insertion loss of the device as the absorption coefficient for cGST is much larger than that for aGST. For optical phase modulation (with Δn_{eff} being the effective index change), we define the optical figure of merit $\text{FOM2} =$

$\Delta n_{\text{eff}}/\kappa_{\text{effa}}$. As both figures of merit do not strongly depend on the dimensions of the silicon rib [38], only the influence of the size of the GST is discussed here while the width w_{si} and height (h_{s}) of the slab are fixed to be 450 nm and 50 nm, respectively. Figure 3(a) shows the variation of the attenuation coefficient and the corresponding FOM1 of the hybrid waveguide concerning the width w_{gst} of GST geometry for aGST and cGST. One can find the attenuation coefficient for aGST increases linearly while the attenuation coefficient for cGST increases rapidly at small w_{gst} and then saturate. The largest reachable FOM1 in this figure is ~ 200 , with the GST dimensions of $w_{\text{gst}} = 70$ nm. Figure 3(b) shows the effective index and FOM2 of the hybrid waveguide with respect to the width w_{gst} . As expected, the n_{eff} for cGST changes by a large amount, while the n_{eff} with aGST remains almost unchanged due to the relatively small index difference between silicon and GST in its amorphous phase. Therefore, the optical mode of the phase-change waveguide with aGST is quite similar to that of a silicon ridge waveguide. In contrast, the optical characteristic of the phase-change waveguide with cGST is very different from those of conventional silicon rib waveguides. From the figure, the largest change in effective index and its corresponding FOM2 accessible with the proposed waveguide is $\Delta n_{\text{eff}} = 1.44$ and FOM2 ~ 250 , and it can be achieved with the GST width of $w_{\text{gst}} = 80$ nm.

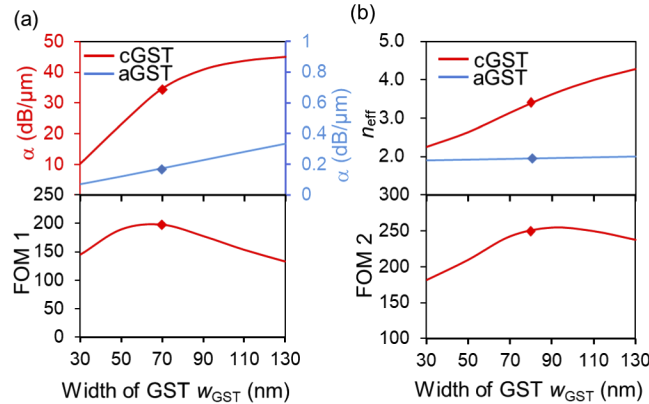


Fig. 3. (a) Attenuation coefficient ($\alpha = 4\pi\kappa_{\text{eff}}/\lambda$, $\lambda = 1550$ nm) and (b) the effective refractive index (n_{eff}) of the hybrid waveguide as a function of the width of the GST with w_{GST} . Here, the width and height of the silicon rib are fixed to be 450 nm and 50 nm, respectively. The marked dots correspond to the structure with largest FOMs denote the adopted waveguide geometry for the following analysis.

3. EA optical modulator

Based on the proposed phase-change waveguide, an optical EA modulator is designed to control the insertion loss and modulate the amplitude of the optical signal passing through the waveguide. Figure 4(a) presents the perspective view of the proposed EA optical modulator. It consists of a 450-nm-wide, and 250-nm-thick silicon waveguide on top of a 3- μm -thick buried oxide. A thin layer of GST with a width of $w_{\text{GST}}=70$ nm and a thickness of $h_{\text{GST}}=200$ nm with a certain length (L) is placed in the center of the slot region of the rib waveguide.

When the GST is in the amorphous state (i.e., ON), the input light propagates through the active segment, experiencing a relatively small optical attenuation [Fig. 4(b)]. With the phase transition to the crystalline phase (i.e., OFF), the hybrid mode hardly propagates and is significantly attenuated. Considering the modulator performances in terms of the ON/OFF extinction ratio (ER, defined as the ratio of the output power between two state), device footprint, and insertion losses (ILs), the waveguide length of $L = 1$ μm is chosen. Almost no signal is transmitted to the

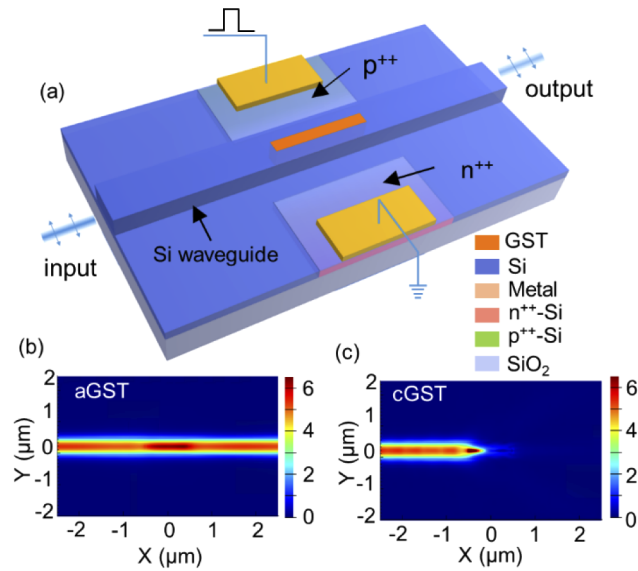


Fig. 4. (a) Schematic of the perspective view of the proposed EA modulator. (b, c) The normalized optical field intensity distribution of the switch for (b) aGST and (c) cGST simulated by the 3D finite-difference time-domain method (Lumerical) at a wavelength of 1550 nm.

output port [Fig. 4(c)]. Figure 5(a) exhibits ER and ILs of the modulator from 1550 nm to 1600 nm. The ER and IL_{ON} at $\lambda = 1550$ nm is 17 dB and 0.2 dB, respectively. In the entire wavelength range of 1500 nm to 1600 nm, the ER is > 15 dB. We use the modulator optical power penalty to access the modulator, which is defined as

$$\text{penalty} = \frac{P_{on} - P_{off}}{2 \times P_{in}}, \quad (1)$$

where P_{on} and P_{off} are optical powers at “ON” and “OFF” states and P_{in} denote the input optical power of the modulator. In Fig. 5(b), power penalty is plotted as a function of the wavelength, where power penalty as low as < 3.5 dB is achieved across the whole range.

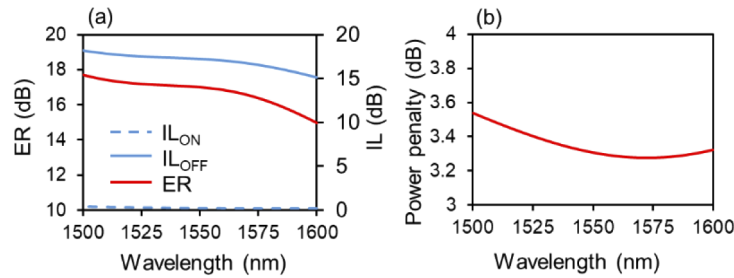


Fig. 5. (a) ON/OFF extinction ratio (ER), insertion losses (IL_{OFF} and IL_{ON}) and (b) Power penalty as a function of wavelength along the propagation length of 1 μ m.

4. DC optical switch

We then employ the proposed phase-change waveguide to form a DC 1×2 electro-optic switch, in which the large effective index difference between the optical modes in cGST and aGST

is utilized to control the power coupling between the input waveguide and each of the output waveguides. Figure 6(a) shows the schematic of the 1×2 DC optical switch, consisting of an asymmetric coupling region with a conventional silicon ridge waveguide and the proposed hybrid phase-change waveguide. When the GST is in the low-loss amorphous state, the optimized structure of the silicon waveguide and the phase-change waveguide can meet the phase-matching condition, inducing the complete power transfer between the input waveguide and the phase-change waveguide [Fig. 6(b)]. With the GST in the lossy crystalline state, the phase-matching condition is broken due to the substantial modification of the optical mode in the hybrid waveguide. As a result, light is diverted away from the phase-change waveguide forming the bar state of the switch with low attenuation ensured by minimal optical field interaction with the lossy phase-change waveguide [Fig. 6(c)].

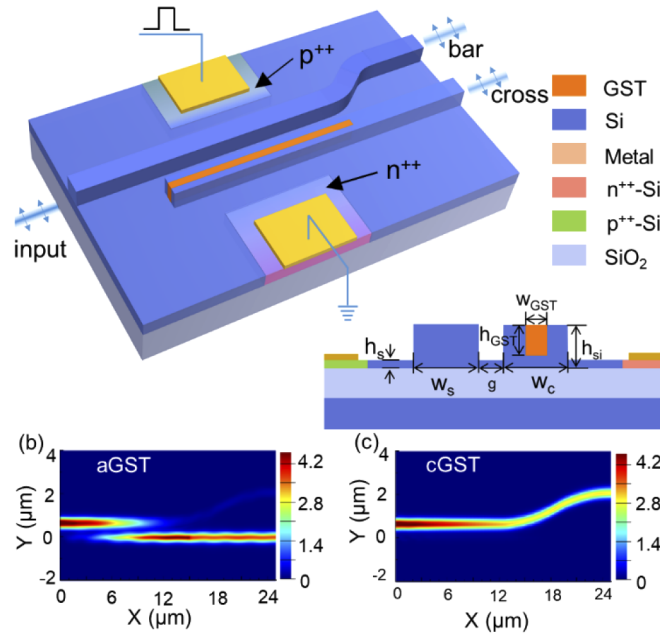


Fig. 6. (a) Schematic of the 1×2 DC switch; (b, c) The normalized optical field intensity distribution of the switch for (b) aGST and (c) cGST simulated by the 3D finite-difference time-domain method (Lumerical) at 1550 nm.

The width of the input silicon waveguide is chosen as $W_s = 500$ nm to ensure a single TM mode. The width of the phase-change waveguide is optimally selected as $W_c = 410$ nm so that the phase-matching condition could be satisfied for aGST when the width of GST is set to be $W_{\text{GST}} = 80$ nm according to the above analysis. Therefore, the input TM-polarized light will be evanescently coupled to the cross port entirely with an appropriate coupling length. Next, the characteristics of the coupling region are studied when varying the gap (g) between the silicon waveguide and phase-change waveguide. There exists a trade-off between the coupling length (L_c) and the insertion loss in the crystalline state (IL_{cGST}). IL_{cGST} is defined as

$$\text{IL}_{\text{cGST}} = L_c \times \alpha_{\text{cGST}2}, \quad (2)$$

where L_c and $\alpha_{\text{cGST}2}$ denote the optimal coupling length corresponding to a specific g and attenuation loss of the second order supermode with the optical energy mainly distributed in silicon. Figure 7(a) shows the L_c and IL_{cGST} as a function of the gap. As the gap increases, the coupling length in the amorphous state increases, while the insertion loss in the crystalline state

decreases due to the weak evanescent coupling between the two waveguides. A moderate g of 200 nm is chosen to ensure the reliable fabrication of the coupling region. The coupling length given by $L_c = \lambda_0/2(n_{aGST1} - n_{aGST2})$ is thus calculated as compact as $\sim 15 \mu\text{m}$, where n_{aGST1} and n_{aGST2} are, respectively, the effective indices of the first-order (even) and second-order (odd) supermodes in the two-waveguide system, $\lambda_0 = 1550 \text{ nm}$ is the wavelength.

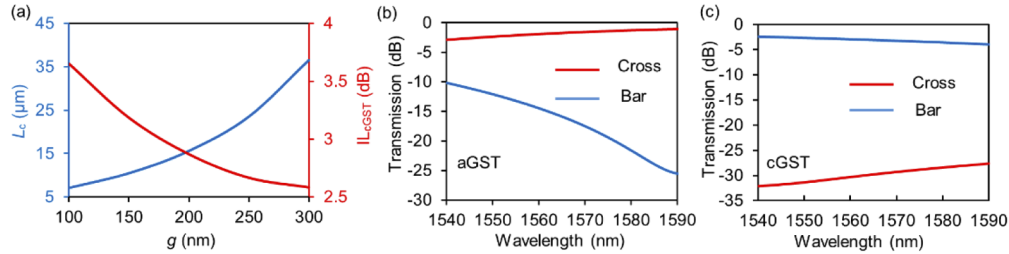


Fig. 7. (a) Coupling length of the maximum transmission in the amorphous state and insertion loss in the crystalline state as a function of g ; Calculated transmission spectrum at the cross and bar ports for (b) aGST and (c) cGST.

Figures 7(b) and 7(c) show the calculated transmission spectral response of the 1×2 DC switch in both states. When the GST is in the amorphous state, the optical switch attains a small $IL < 2.8 \text{ dB}$ and CT from -7.2 dB to -24.5 dB over the wavelength range of 1540–1590 nm. For the crystalline state, since almost no evanescent coupling occurs due to the phase mismatch, the spectral response to the input light is quite flat and broadband. The corresponding IL and CT are $< 4 \text{ dB}$ and $< -23.7 \text{ dB}$ across the whole wavelength range.

5. Thermal simulation

In this section, we built up a comprehensive 2-D finite element model to simulate the electrical switching of the photonic devices with silicon PIN heaters based on COMSOL Multiphysics [38]. The schematic of the model is consistent with the actual device, in which a GST layer is embedded into a silicon rib waveguide. The material parameters set by the simulation are shown in Table 1. The crystallization process is a thermodynamic mechanism, which requires the phase change material to be heated above its crystallization temperature ($T_g = 413 \text{ K}$). The amorphization process requires heating the material above its melting temperature ($T_m = 891 \text{ K}$), and then quenching the material faster than the crystallization speed, resulting it in an amorphous state.

Table 1. Materials parameters used for simulations.^a

	n	κ	K ($\text{Wm}^{-1}\text{K}^{-1}$)	C_p ($\text{J kg}^{-1}\text{K}^{-1}$)	ρ (kg m^{-3})
aGST	3.8884 [20]	0.024694 [20]	0.19 [40]	213 [41]	5870 [42]
cGST	6.630 [20]	1.0888 [20]	0.57 [40]	199 [41]	6270 [42]

^a n , refractive index. κ , Extinction coefficient. k , the thermal conductivity. C_p , the heat capacity at constant pressure. ρ , density. T , temperature. All optical parameters are for 1550 nm.

We first analyze the GST crystallization process in EA modulator, corresponding to the transition from ON state to the OFF state. Figure 8(a) shows the temperature distribution of the modulator cross section at the end of a pulse, while Figs. 8(b)–8(c) shows the temperature profiles along the y -axis and z -axis, respectively. Our results indicate that the complete crystallization process can be achieved by a pulse of 5 V ($\sim 10 \text{ mW}$) for 180 ns, raising the GST temperature above the crystallization temperature ($T_g = 413 \text{ K}$) required for phase transformation and below

the melting temperature ($T_m = 891$ K). The energy consumed during the process is estimated to 890 pJ (~ 64 aJ/nm³). It can be improved by optimizing its electrical contact to increase the number of free carriers. Next, we initiate the amorphization process, in which the device goes from OFF to ON state. A high-power pulse is required to raise the temperature of GST above the melting temperature, and then quickly quench it below the crystallization temperature to form a disordered state with low optical constant. Figure 8(d) shows the cross-sectional temperature distribution of the modulator in the amorphization process. The temperature profile along the y axis and z axis is illustrated in Figs. 8(e)–8(f) at the end of a pulse, and the temperature in GST rises to 1200 K, which is higher than its melting temperature. A pulse of 10 V (~ 40 mW) for 30 ns is applied to the device to complete the amorphization process. The energy consumption for the phase transition is 500 pJ (~ 36 aJ/nm³), which is much less than that in the crystallization process.

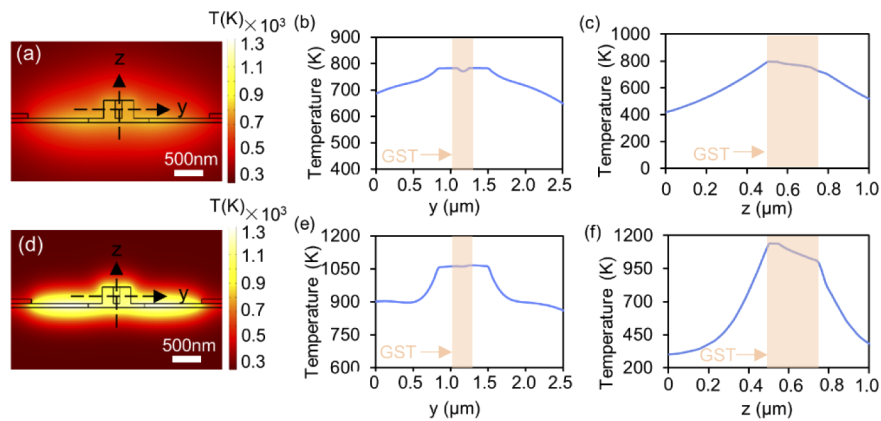


Fig. 8. (a) Simulated temperature (T) profile of the EA modulator in crystalline process. Temperature profile along the (b) y axis and (c) z axis in (a). (d) Simulated temperature (T) profile in amorphous process. Temperature profile along the (e) y axis and (f) z axis in (d). The orange-shaded areas in (b, c, e, f) represent the position of the GST film.

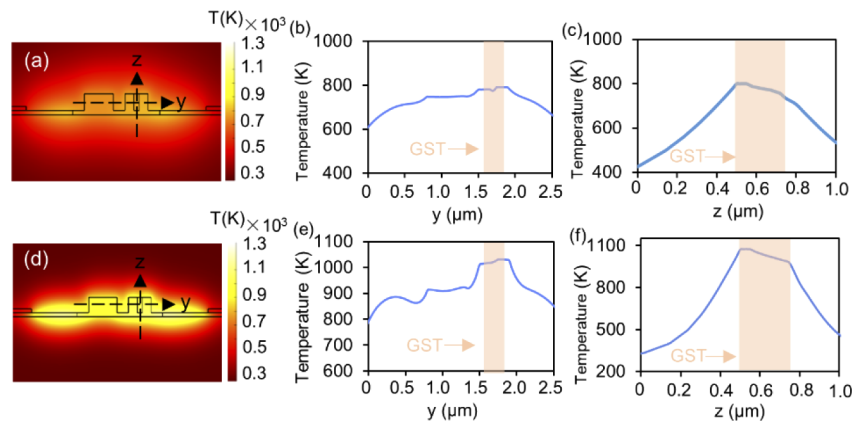


Fig. 9. (a) Simulated temperature (T) profile of the 1×2 DC optical switch in crystalline process. Temperature profile along the (b) y axis and (c) z axis in (a). (d) Simulated temperature (T) profile in amorphous process. Temperature profile along the (e) y axis and (f) z axis in (d). The orange-shaded areas in (b, c, e, f) represent the position of the GST film.

We also investigate the similar thermal analysis on the 1×2 DC switch. Figure 9(a) shows the calculated temperature distributions of the device at the end of a pulse and presents the corresponding temperature profiles along the y axis and z axis, as shown in Figs. 9(b)–9(c). A pulse of 6V (~ 12 mW) for 200 ns duration is required to induce the complete crystallization with the energy consumption of ~ 1.2 nJ (~ 75 aJ/nm³). In the amorphization process, a pulse of 10V (~ 30 mW) for 55 ns is applied to the device with the energy consumption of crystallization is 687 pJ (~ 43 aJ/nm³). The high energy consumption compared to the modulator in both the crystalline and amorphous process can be attributed to a long distance between the left metal contact and the GST part. In particular, the temperature distributions [Fig. 9(d)] and corresponding temperature profiles [Fig. 9(e)–9(f)] along the y and z axis in the amorphous process indicate that the GST is almost uniformly heated in the horizontal direction except for the edges.

6. Conclusion

In summary, a nanogap-enhanced phase-change waveguide with PIN diode silicon heaters is proposed. By optimizing the waveguide dimensions, the effective index and the propagation loss variations as high as $\Delta n_{\text{eff}} = \sim 1.2$, and $\Delta\alpha = \sim 30$ dB/ μm , respectively, are obtained upon phase transition. Benefiting from the considerable change in optical phase and attenuation, two examples of the active optical devices based on the phase-change waveguide were then presented; an optical EA modulator and a 1×2 DC optical switch. Finite-difference time-domain simulation of the EA modulator shows a high extinction ratio of ~ 17 dB at 1550 nm with an active segment of $0.014 \mu\text{m}^3$. By exploiting the high optical contrast of PCMs and asymmetric DC design, we demonstrated compact ($\sim 15 \mu\text{m}$) nonvolatile silicon 1×2 optical switch with an insertion loss of < 4 dB and broadband (over 50 nm with small crosstalk < -7.2 dB) operations. With the design of nanogap-enhanced phase-change waveguide, this work represents an important improvement on nonvolatile modulating/switching technology, which can find numerous applications for optical communications, microwave photonics, and electronically programmable reconfigurable photonics.

Funding

National Natural Science Foundation of China (61875099); Natural Science Foundation of Zhejiang Province (LGJ18F050001, LY18F050005); Natural Science Foundation of Ningbo (202003N4007); National Science Foundation (1640986, 2003509); ONR-YIP Award; K. C. Wong Magna Fund at Ningbo University.

Disclosures

The authors declare no conflicts of interest.

References

1. R. Won, "Integrating silicon photonics," *Nat. Photonics* **4**(8), 498–499 (2010).
2. A. Rickman, "The commercialization of silicon photonics," *Nat. Photonics* **8**(8), 579–582 (2014).
3. Y. Arakawa, T. Nakamura, Y. Urino, and T. Fujita, "Silicon photonics for next generation system integration platform," *IEEE Commun. Mag.* **51**(3), 72–77 (2013).
4. L. Zhuang, C. G. H. Roeloffzen, M. Hoekman, K.-J. Boller, and A. J. Lowery, "Programmable photonic signal processor chip for radiofrequency applications," *Optica* **2**(10), 854–859 (2015).
5. D. Pérez, I. Gasulla, L. Crudgington, D. J. Thomson, A. Z. Khokhar, K. Li, W. Cao, G. Z. Mashanovich, and J. Capmany, "Multipurpose silicon photonics signal processor core," *Nat. Commun.* **8**(1), 636 (2017).
6. W. Liu, M. Li, R. S. Guzzon, E. J. Norberg, J. S. Parker, M. Lu, L. A. Coldren, and J. Yao, "A fully reconfigurable photonic integrated signal processor," *Nat. Photonics* **10**(3), 190–195 (2016).
7. W. Bogaerts, P. De Heyn, T. Van Vaerenbergh, K. De Vos, S. Kumar Selvaraja, T. Claes, P. Dumon, P. Bienstman, D. Van Thourhout, and R. Baets, "Silicon microring resonators," *Laser Photonics Rev.* **6**(1), 47–73 (2012).
8. S. Chen, Y. Shi, S. He, and D. Dai, "Low-loss and broadband 2×2 silicon thermo-optic Mach-Zehnder switch with bent directional couplers," *Opt. Lett.* **41**(4), 836–839 (2016).

9. L. Lu, S. Zhao, L. Zhou, D. Li, Z. Li, M. Wang, X. Li, and J. Chen, "16 × 16 non-blocking silicon optical switch based on electro-optic Mach-Zehnder interferometers," *Opt. Express* **24**(9), 9295–9307 (2016).
10. S. Abdollahramezani, O. Hemmatyar, H. Taghinejad, A. Krasnok, Y. Kiarashinejad, M. Zandehshahvar, A. Alù, and A. Adibi, "Tunable nanophotonics enabled by chalcogenide phase-change materials," *Nanophotonics* **9**(5), 1189–1241 (2020).
11. M. Wuttig, H. Bhaskaran, and T. Taubner, "Phase-change materials for non-volatile photonic applications," *Nat. Photonics* **11**(8), 465–476 (2017).
12. K. Shportko, S. Kremers, M. Woda, D. Lencer, J. Robertson, and M. Wuttig, "Resonant bonding in crystalline phase-change materials," *Nat. Mater.* **7**(8), 653–658 (2008).
13. M. Wuttig and N. Yamada, "Phase-change materials for rewriteable data storage," *Nat. Mater.* **6**(11), 824–832 (2007).
14. H. P. Wong, S. Raoux, S. Kim, J. Liang, J. P. Reifenberg, B. Rajendran, M. Asheghi, and K. E. Goodson, "Phase Change Memory," *Proc. IEEE* **98**(12), 2201–2227 (2010).
15. S. Raoux, F. Xiong, M. Wuttig, and E. Pop, "Phase change materials and phase change memory," *MRS Bull.* **39**(8), 703–710 (2014).
16. D. Loke, T. H. Lee, W. J. Wang, L. P. Shi, R. Zhao, Y. C. Yeo, T. C. Chong, and S. R. Elliott, "Breaking the Speed Limits of Phase-Change Memory," *Science* **336**(6088), 1566–1569 (2012).
17. C. Ríos, N. Youngblood, Z. Cheng, M. Le Gallo, W. H. P. Pernice, C. D. Wright, A. Sebastian, and H. Bhaskaran, "In-memory computing on a photonic platform," *Sci. Adv.* **5**(2), eaau5759 (2019).
18. J. Feldmann, M. Stegmaier, N. Gruhler, C. Ríos, H. Bhaskaran, C. D. Wright, and W. H. P. Pernice, "Calculating with light using a chip-scale all-optical abacus," *Nat. Commun.* **8**(1), 1256 (2017).
19. Z. Cheng, C. Ríos, W. H. P. Pernice, C. D. Wright, and H. Bhaskaran, "On-chip photonic synapse," *Sci. Adv.* **3**(9), e1700160 (2017).
20. J. Zheng, A. Khanolkar, P. Xu, S. Colburn, S. Deshmukh, J. Myers, J. Frantz, E. Pop, J. Hendrickson, J. Doylend, N. Boechler, and A. Majumdar, "GST-on-silicon hybrid nanophotonic integrated circuits: a non-volatile quasi-continuously reprogrammable platform," *Opt. Mater. Express* **8**(6), 1551–1561 (2018).
21. P. Xu, J. Zheng, J. K. Doylend, and A. Majumdar, "Low-Loss and Broadband Nonvolatile Phase-Change Directional Coupler Switches," *ACS Photonics* **6**(2), 553–557 (2019).
22. M. Rudé, J. Pello, R. E. Simpson, J. Osmond, G. Roelkens, J. J. G. M. van der Tol, and V. Pruneri, "Optical switching at 1.55 μm in silicon racetrack resonators using phase change materials," *Appl. Phys. Lett.* **103**(14), 141119 (2013).
23. M. Stegmaier, C. Ríos, H. Bhaskaran, C. D. Wright, and W. H. P. Pernice, "Nonvolatile All-Optical 1 × 2 Switch for Chipscale Photonic Networks," *Adv. Opt. Mater.* **5**(1), 1600346 (2017).
24. C. Wu, H. Yu, H. Li, X. Zhang, I. Takeuchi, and M. Li, "Low-Loss Integrated Photonic Switch Using Subwavelength Patterned Phase Change Material," *ACS Photonics* **6**(1), 87–92 (2019).
25. H. Zhang, L. Zhou, L. Lu, J. Xu, N. Wang, H. Hu, B. M. A. Rahman, Z. Zhou, and J. Chen, "Miniature Multilevel Optical Memristive Switch Using Phase Change Material," *ACS Photonics* **6**(9), 2205–2212 (2019).
26. K. Kato, M. Kuwahara, H. Kawashima, T. Tsuruoka, and H. Tsuda, "Current-driven phase-change optical gate switch using indium–tin-oxide heater," *Appl. Phys. Express* **10**(7), 072201 (2017).
27. F. D. Leonardis, R. Soref, V. M. N. Passaro, Y. Zhang, and J. Hu, "Broadband Electro-Optical Crossbar Switches Using Low-Loss Ge₂Sb₂Se₄Te₁ Phase Change Material," *J. Lightwave Technol.* **37**(13), 3183–3191 (2019).
28. H. Liang, R. Soref, J. Mu, A. Majumdar, X. Li, and W. Huang, "Simulations of Silicon-on-Insulator Channel-Waveguide Electrooptical 2 × 2 Switches and 1 × 1 Modulators Using a Ge₂Sb₂Te₅ Self-Holding Layer," *J. Lightwave Technol.* **33**(9), 1805–1813 (2015).
29. B. Janjan, M. Miri, A. Zarifkar, and M. Heidari, "Design and Simulation of Compact Optical Modulators and Switches Based on Si-VO₂-Si Horizontal Slot Waveguides," *J. Lightwave Technol.* **35**(14), 3020–3028 (2017).
30. Z. Yu, J. Zheng, P. Xu, W. Zhang, and Y. Wu, "Ultracompact Electro-Optical Modulator-Based Ge₂Sb₂Te₅ on Silicon," *IEEE Photonics Technol. Lett.* **30**(3), 250–253 (2018).
31. V. R. Almeida, Q. Xu, C. A. Barrios, and M. Lipson, "Guiding and confining light in void nanostructure," *Opt. Lett.* **29**(11), 1209–1211 (2004).
32. L. Zhang, Q. Lin, Y. Yue, Y. Yan, R. G. Beausoleil, and A. E. Willner, "Silicon waveguide with four zero-dispersion wavelengths and its application in on-chip octave-spanning supercontinuum generation," *Opt. Express* **20**(2), 1685–1690 (2012).
33. M. Zhu, H. Liu, X. Li, N. Huang, Q. Sun, J. Wen, and Z. Wang, "Ultrabroadband flat dispersion tailoring of dual-slot silicon waveguides," *Opt. Express* **20**(14), 15899–15907 (2012).
34. S. Serna, H. Lin, C. Alonso-Ramos, C. Lafforgue, X. Le Roux, K. A. Richardson, E. Cassan, N. Dubreuil, J. Hu, and L. Vivien, "Engineering third-order optical nonlinearities in hybrid chalcogenide-on-silicon platform," *Opt. Lett.* **44**(20), 5009–5012 (2019).
35. S. R. Mirnaziry, C. Wolff, M. J. Steel, B. J. Eggleton, and C. G. Poulton, "Stimulated Brillouin scattering in silicon/chalcogenide slot waveguides," *Opt. Express* **24**(5), 4786–4800 (2016).
36. P. Xu, J. Zheng, J. Zhou, Y. Chen, C. Zou, and A. Majumdar, "Multi-slot photonic crystal cavities for high-sensitivity refractive index sensing," *Opt. Express* **27**(3), 3609–3616 (2019).
37. E. Luan, H. Yun, M. Ma, D. M. Ratner, K. C. Cheung, and L. Chrostowski, "Label-free biosensing with a multi-box sub-wavelength phase-shifted Bragg grating waveguide," *Biomed. Opt. Express* **10**(9), 4825–4838 (2019).

38. J. Zheng, S. Zhu, P. Xu, S. Dunham, and A. Majumdar, "Modeling Electrical Switching of Nonvolatile Phase-Change Integrated Nanophotonic Structures with Graphene Heaters," *ACS Appl. Mater. Interfaces* **12**(19), 21827–21836 (2020).
39. J. Zheng, Z. Fang, C. Wu, S. Zhu, P. Xu, J. K. Doylend, S. Deshmukh, E. Pop, S. Dunham, M. Li, and A. Majumdar, "Nonvolatile Electrically Reconfigurable Integrated Photonic Switch Enabled by a Silicon PIN Diode Heater," *Adv. Mater.* **32**(31), 2001218 (2020).
40. H.-K. Lyeo, D. G. Cahill, B.-S. Lee, J. R. Abelson, M.-H. Kwon, K.-B. Kim, S. G. Bishop, and B.-k. Cheong, "Thermal conductivity of phase-change material Ge₂Sb₂Te₅," *Appl. Phys. Lett.* **89**(15), 151904 (2006).
41. A. Pirovano, A. L. Lacaita, A. Benvenuti, F. Pellizzer, S. Hudgens, and R. Bez, "Scaling analysis of phase-change memory technology," in *IEEE International Electron Devices Meeting 2003* (2003), pp. 29.26.21–29.26.24.
42. W. K. Njoroge, H.-W. Wöltgens, and M. Wuttig, "Density changes upon crystallization of Ge₂Sb₂.04Te_{4.74} films," *J. Vac. Sci. Technol., A* **20**(1), 230–233 (2002).